Scripta Materialia 247 (2024) 116115

Contents lists available at ScienceDirect

Scripta Materialia

journal homepage: www.journals.elsevier.com/scripta-materialia

Correlative synchrotron absorption edge tomography and microtomography provide insights into the effect of element distribution within intermetallic phases on the fracture behaviour of cast Al-Si alloys

Katrin Bugelnig [a,*], Holger Germann [b], Thomas Steffens [b], Fabian Wilde [c], Guillermo Requena [a,d]

[a] Institute for Materials Research, German Aerospace Centre, Linder Höhe, Cologne 51147, Germany
[b] KS Kolbenschmidt GmbH, Karl-Schmidt-Straße, Neckarsulm 74172, Germany
[c] Helmholtz-Zentrum Hereon, Zentrum für Material- und Küstenforschung GmbH, Max-Planck-Straße 1, 21502, Geesthacht, Germany
[d] Metallic Structures and Materials Systems for Aerospace Engineering, RWTH Aachen University, Aachen 52062, Germany

ARTICLE INFO

Keywords:
Three-dimensional tomography
Synchrotron radiation
Aluminum alloys
Mechanical properties
3d elemental distribution

ABSTRACT

A combined 3D investigation of elemental distribution and tensile fracture behaviour was carried out using synchrotron x-ray micro-tomography and absorption edge tomography for two near eutectic cast Al-Si-Cu-Ni alloys. Absorption edge tomography allowed the identification of intermetallics three-dimensionally based on the Cu/Ni distribution and morphology of the phases. In addition, inhomogeneities in the distributions, especially on the surface of intermetallics, were revealed by this technique. A correlation of the post-mortem state with the 3D Cu and Ni distributions showed that the main crack tends to propagate along interfaces between different types of intermetallics, while local inhomogeneities in element distribution within intermetallics acted as crack deflection sites.

The microstructure of cast near-eutectic Al-Si alloys for automotive applications consists of highly interconnected 3D hybrid networks of eutectic/primary Si and multi-component intermetallics embedded in an age hardenable α – Al-matrix. Their interconnectivity, morphology, distribution and composition play a crucial role on damage behaviour, as shown in previous works by the authors and others [1–4]. Damage during tensile deformation and thermo-mechanical fatigue of these alloys initiates in the form of microcracks through primary Si clusters and propagates further through intermetallics such as γ-Al_7Cu_4Ni, δ-Al_3NiCu and β-Al_5FeSi [1,2,4-6]. Morphological changes of Cu-rich intermetallics induced by solution treatment at 500 °C/4 h have shown to reduce local connectivity of the 3D hybrid network of an AlSi12Cu4Ni2 alloy, resulting in reduced strength and increased elongation at fracture during RT deformation [2]. Ni contents above 2 wt.% resulted in the formation of the needle-like δ phase, leading to an increase of local connectivity of the 3D network in an AlSi12Cu4Ni3Mg alloy and earlier damage formation during deformation at 300 °C [1]. Efforts have been made to reveal the 3D elemental distribution within intermetallics in cast Al-Si alloys: e.g. Asghar et al. [7] used light optical tomography for 3D visualization of individual intermetallics. Liu et al. used transmission X-ray microscopy to reveal the 3D distribution of Ni and Cu within a Ni-Cu-rich intermetallic in a cast AlSi10Cu5Ni2 alloy [8]. However, these techniques are destructive or restricted to small volumes and do not allow a direct correlation between damage and 3D elemental distribution. On the other hand, dual-energy K-edge subtraction imaging and synchrotron X-ray microtomography (sXCT) have been applied to study the evolution of the spatial distribution of Cu during solution treatment in an Al-Si-Cu alloy [9,10] and also on other Al-based materials such as Al-Zn-Mg foams [11]. For Al-Si-Cu alloys, the beneficial effect of homogenization during solutionizing on mechanical properties, as revealed by the Cu distribution, has been mainly attributed to a reduction in the growth rate of micropores that promote crack initiation and propagation [9]. However, the effect of the 3D element distribution in intermetallics and their inhomogeneities on the fracture behaviour of Al-Si alloys, in which porosity plays a minor role [2], remains to be investigated. In this study, synchrotron x-ray micro-tomography and synchrotron absorption edge tomography (sAET) were applied to tensile specimens of near-eutectic Al-Si alloys to enable the combined 3D investigation of elemental distribution, phases morphology and damage as a function of alloy composition.

Two cast near-eutectic Al-Si alloys with different Cu, Ni and Mg contents were investigated (Table 1).

* Corresponding author.
E-mail address: katrin.bugelnig@dlr.de (K. Bugelnig).

https://doi.org/10.1016/j.scriptamat.2024.116115
Received 4 October 2023; Received in revised form 19 March 2024; Accepted 2 April 2024
Available online 12 April 2024

Table 1
labelling and chemical composition of investigated alloys.

Alloy	labelling	approx. chem. composition [wt.%]					
		Al	Si	Cu	Ni	Mg	Fe
AlSi12Cu3Ni2	1232	bal.	12.3	~3	~ 2	< 1	~ 0.4
AlSi12Cu4Ni2Mg	12421	bal.	12.5	~ 4	~ 2	~ 1	~ 0.4

The designations 1232 and 12421 will be used hereafter for AlSi12Cu3Ni2 and AlSi12Cu4Ni2Mg, respectively. The alloys were produced by gravity die casting by Kolbenschmidt GmbH and their composition was measured by mass spectroscopy. sXCT and sAET were performed at the beamline P05, operated by Helmholtz-Zentrum Hereon at the PETRA III/DESY in Hamburg, Germany [12]. Samples were spark eroded to a flat dogbone-shaped geometry with a thickness of 150 - 200 μm to ensure sufficient X-ray transmission for tomographic scans at lower energies (gauge volume ~ 1 × 0.2 × 2 mm^3; Supplementary Figure S1 a)) [13]. No further sample preparation like surface polishing was performed. An in-situ tensile rig available at the beamline P05 was used in the experiments (Supplementary Figure S1 b)). First, sAET was performed below and above the K-edges of Ni (8.310 keV and 8.350 keV, respectively) and Cu (8.960 keV and 9.0 keV, respectively). Then, the energy was increased to 20 keV, at which point sXCT was performed of the tensile specimen in initial condition and post-mortem condition at RT. Table 2 shows the parameters for the sXCT and sAET scans.

Finally, the 3D tomographic data was analysed to determine the effect of 3D elemental distribution on fracture behaviour. The softwares Fiji [14] and Avizo Fire were used for 3D data processing and analysis. To obtain the 3D elemental distribution of Ni and Cu, the tomographic scans acquired at energies above and below the absorption K-edges of each element were first normalized with respect to the beam intensity and then subtracted from each other after pixel-accurate registration [8, 15]. For noise reduction a 3D median filter was applied.

To gain understanding of the phase formation, composition and distribution thermodynamic simulations were performed using the CALPHAD method, using the software Thermo-Calc 2023a [16] and the TCAL7 database for Al. Scheil-Gulliver calculations showed that the phase fraction and composition of a phase depend on the contents and ratios of Ni:Cu, Ni:Fe and Cu:Mg (Supplementary Figure S2). A more detailed description can be found in the supplements. However, the phase fractions and their composition may vary from theoretical estimations as the real casting process can result in metastable phases and inhomogeneities in phase composition. It is therefore essential to identify experimentally the 3D distribution of intermetallic-forming elements.

SEM micrographs and EDX maps (Supplementary Figure S3) reveal the presence of several Al-Cu-Ni, Al-Fe-Ni, Al-Cu and Al-Cu-Mg-Si rich intermetallics in both studied alloys. Point EDX measurements and correlation with literature [17–21] allowed an identification based on elemental concentrations as: Si, θ-Al_2Cu (25 - 53 wt.% Cu), δ-$Al_3(Cu,Ni)_2$ (~ 30–60 wt.% Ni, ~ 5–31 wt.% Cu), T-Al_9FeNi (4.5 – 14 wt.% Fe, 18 - 28 wt.% Ni), β-Al_5FeSi (25 – 30 wt.% Fe, 12 – 15 wt.% Si), π-$Al_8FeMg_3Si_6$ (~ 11 wt.% Fe, 14 wt.% Mg, 33 wt.% Si) and α-$Al_{15}(Fe,Mn)_3Si_2$. The alloy 12421 additionally contains Mg_2Si (~ 63 wt.% Mg, 36 wt.% Si) and Q-$Al_5Si_6Cu_2Mg_8$ (~ 20 wt.% Cu, 31 wt.% Mg, 27 wt.% Si), and also has a larger fraction of γ-Al_7Cu_4Ni (~ 38 – 50 wt.% Cu, 11.5 – 22 wt.% Ni) owing to the higher content of Cu in this alloy. These phases have also been frequently observed to form in commercial alloys within the Al-Si-Cu-Ni-Fe-Mg-Mn system, e.g. [17–21]. Qualitatively, there also appears to be a transition towards more needle/plate-like morphologies of the Cu-Ni-rich intermetallics in alloy 12421 compared to alloy 1232 which also exhibits this type of intermetallics in smaller, more compact morphology.

Table 2
Parameters for sXCT and sAET.

	E [keV]	voxel size [$μm^3$]	sample-to-detector distance [mm]	Nr. of proj.	exposure time [ms/proj.]	total scan time [min]
sXCT	20	1.28	60	2001	280	14
sAET	8.310/ 8.350 8.960/ 9.000	1.28	60	2001	1050	42

Quantification of the 3D networks of eutectic/primary Si and intermetallics within a large representative 3D volume obtained by sXCT revealed a volume fraction of the hybrid 3D network of 20.6 ± 1 vol.% and 24.8 ± 1.2 vol.% for 1232 and 12421, respectively. The intermetallics volume fraction amounts to 12.4 ± 0.2 vol.% and 18.2 ± 0.5 vol.% for 1232 and 12421, respectively. 3D visualizations of the hybrid networks formed by Si and intermetallics are shown in supplementary Figure S4.

sAET enables element sensitive 3D imaging: As Cu and Ni are present in the γ and δ phases, this technique provides information about the homogeneity of the 3D distribution of these elements and the thermodynamic stability of the phases. Moreover, the β phase can also be identified since it does not contain Ni nor Cu. The α-$Al_{15}(Fe,Mn)_3Si_2$ phase also contains Ni and Cu and can be distinguished by morphology. Si can be distinguished by its grey value in the reconstructed 2D slices. Mg_2Si and Q-$Al_5Si_6Cu_2Mg_8$ can be identified on the basis of their bulky, sponge-like morphology, based on the information obtained from 2D SEM micrographs and the EDX maps as a reference (Supplementary Figure S3). The Al-Fe-Ni rich T phase can be identified by its Ni content and plate-like morphology. Fig. 1 shows representative 2D sXCT slices acquired at an energy of 20 keV (left) and the corresponding distribution of Ni (middle) and Cu (right) obtained by sAET. For alloy 12421 Si, Al-Cu-Ni-, Al-Fe-Ni-, Al-Cu- and Al-Cu-Mg-Si-rich phases could be identified, while Si, Al-Cu-Ni-, Al-Fe-Ni- and Al-Cu-rich phases were found in alloy 1232. Based on their morphology, bulky Al-Cu-Ni-rich phases are more likely to be of the γ type, whereas δ has more needle/plate-like morphologies. On several occasions Al-Cu-rich and Al-Cu-Ni-rich phases, most probably θ, γ, δ, are found adjacent to other Al-Cu-Ni-rich, which may be a consequence of phases that nucleated onto other ones which are known to form earlier during solidification, e.g. γ formed on the surface of δ [20]. Based on information about phase compositions from the TCAL7 database and literature a substitution of Cu → Ni, Cu → Fe and Ni → Fe within ternary AlNi(Cu or Fe) intermetallics can be expected depending on the Ni, Cu and Fe content of the alloy system. Thus, Ni-Fe-rich phases can also serve as nucleation sites for Al-Cu-Ni-rich phases, as it has also been frequently reported, e.g. [20,21].

Fig. 2 shows a 3D visualization of the Cu and Ni distributions as well as both elements superimposed. Histograms of elemental intensity distributions (Supplementary Figure S5) show that alloy 1232 presents very similar intensity for Cu- and Ni-rich regions. Alloy 12421 has a significantly higher Cu content within its intermetallics compared to Ni. In addition, the Cu-rich regions have an intensity that is about 100% larger than those of 1232, whereas the concentration of Ni-rich regions is similar for both alloys. In addition, the Ni-containing intermetallics show more needle/plate-like morphologies compared to the 1232 alloy. There also appear to be inhomogeneities in the Cu and Ni distribution on the surface of the Al-Ni-Cu-rich intermetallics as indicated with orange arrows in the enlarged 3D visualizations in Fig. 2. This is also in agreement with SEM/EDX mappings (Supplementary Figure S6, inhomogeneities indicated by arrows).

A RT tensile test was carried out. The sample was deformed with a constant displacement rate of 1 μm/s for alloy 12421 to investigate the influence of intermetallics, their morphology and their 3D elemental distribution within intermetallics on the fracture behaviour of the alloys. As damage mechanisms during tensile deformation were found to be the same for several cast near-eutectic Al-Si-Cu-Ni-(Mg) alloys at ambient and elevated temperatures in previous works by the authors [1,2], the

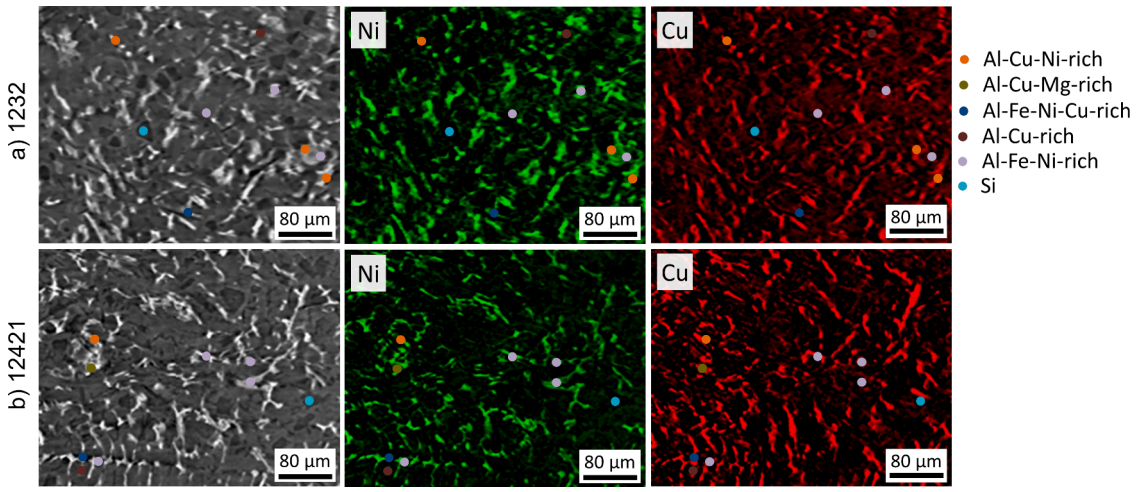

Fig. 1. (left) 2D tomographic slices acquired at energies of 20 keV (optimal condition for tensile tests), and corresponding Ni (middle) and Cu (right) distribution maps determined as the difference between scans acquired below and above the absorption K-edge of each element for a) 1232 and b) 12421. Identified phases are indicated by colour-coded circles.

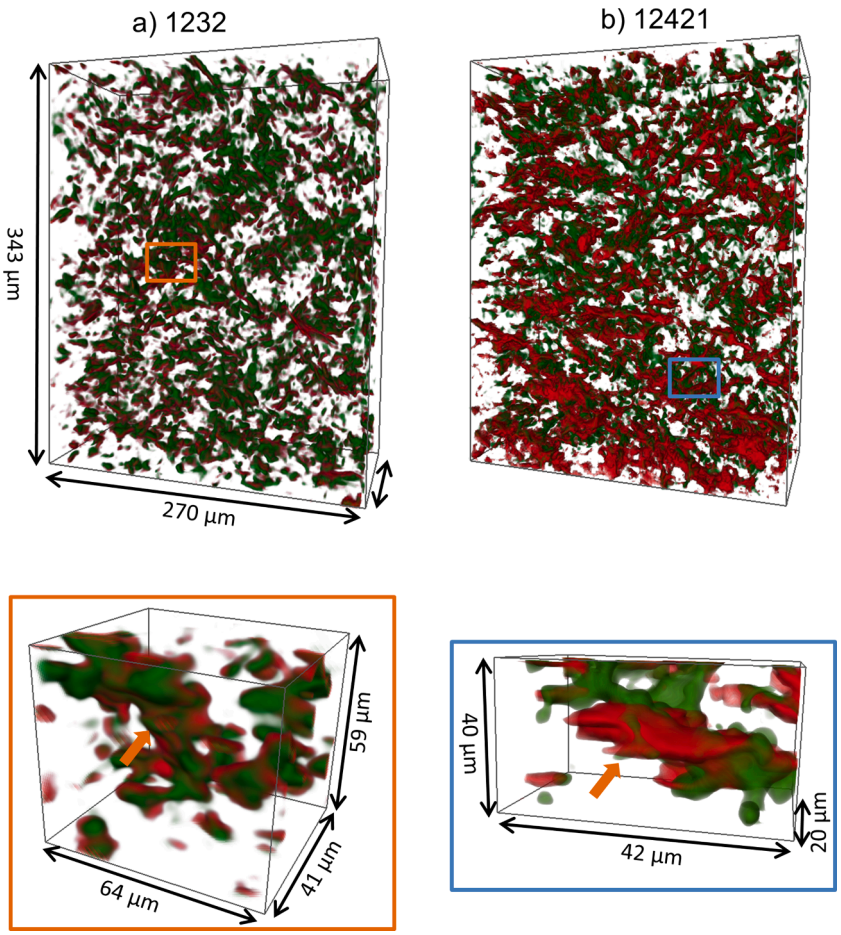

Fig. 2. 3D visualization of the overlapped individual elemental distribution of Cu (red) and Ni (green). The orange and blue rectangles correspond to the enlarged 3D visualized regions below.

results are expected to be representative for this alloys' family. Fig. 3a) shows the stress-strain curve obtained. A rather brittle behaviour with an elongation at fracture of about 0.4% and a maximum tensile strength of ~310 MPa is observed. The high stiffness can be attributed to the observed highly interconnected 3D network of primary rigid phases that has a significant strengthening effect on the material added to the precipitation and solid-solution strengthening, as shown in the authors' previous work and by others [1,2,22]. The results obtained for miniature specimens are in good agreement with mechanical properties given by Kolbenschmidt for standard tensile test specimens at RT, i.e. UTS = 270 MPa, $Rp_{0.2}$ = 230 MPa, A% ~ 0.5%.

Previous studies showed that crack initiation in these alloys typically

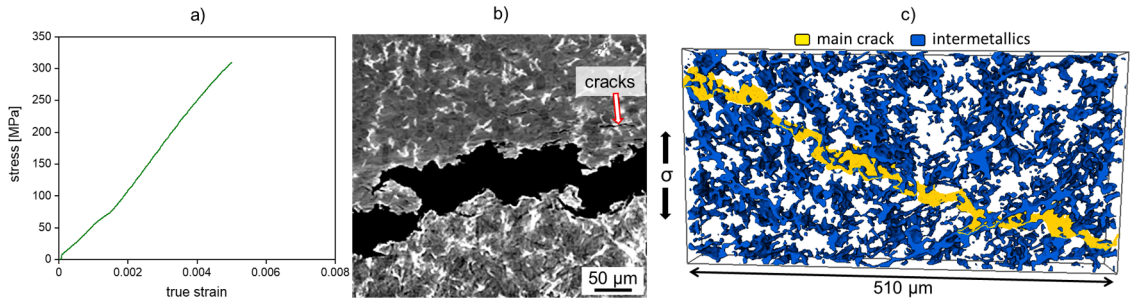

Fig. 3. a) stress-strain curve obtained during a tensile test at RT for 12421; b) reconstructed 2D slice of the post-mortem state and c) corresponding 3D visualization of intermetallics (blue) and the main crack (yellow).

occurs by microcracking through primary silicon particle clusters. Cracking through intermetallics occurs only in the final stages of deformation. Final failure is caused by a coalescence of cracks through primary Si and intermetallics [2]. Crack initiation and accumulation through Si particles has been extensively studied [1,2], now the focus is on the influence of intermetallics on main crack propagation and fracture behaviour. The 2D tomographic slice of the sample in the post-mortem state shown in Fig. 3b) gives a first impression of the role played by the rigid phases (intermetallics and Si) in the propagation of the main crack. The superimposed 3D visualization of the intermetallics (blue) and the main crack (yellow) in Fig. 3c) further emphasises how the main crack propagates through intermetallics rather than the Al-matrix or the matrix/intermetallic interface, typical for this alloy family [2].

A correlation between the 3D elemental distribution and fracture behaviour can now be established. Fig. 4 gives insight into the heterogeneous distribution of the elements Cu and Ni within the intermetallics for both alloys. A variation in Cu and Ni through the thickness of the particles, particularly towards their surface, can be seen at several locations. This can be explained by the relatively fast solidification rates during casting (~ 50 K/min), which do not allow for the complete stabilisation of the intermetallics. Similar observations were reported by Y. Liu et al. [8] for an as-cast AlSi10Cu5Ni2 alloy using transmission X-ray microscopy on a Cu-Ni-containing intermetallic. In addition, the heterogenous elemental concentration within the intermetallics appears to be more pronounced for Cu. This can be explained by the different solubilities of Cu and Ni in the Al-matrix. While Ni, with low solubility, is rejected into the residual liquid during solidification and reaches a local concentration sufficient to form thermally stable intermetallic compounds, Cu, with higher solubility, only contributes to the formation of low-melting Cu-Ni-rich/Cu-rich compounds directly from the residual liquid once it is enriched in Cu. Ni, on the other hand, is assimilated from locally enriched residual liquid from the dissolution of previously formed Ni-rich phases (e.g. ε) [17,20,21,23]. This phenomenon is particularly evident for alloy 12421 (Fig. 4b), probably as a consequence of the formation of a larger fraction of the high Cu-containing γ phase in addition to the δ phase, which generally has similar Cu/Ni contents. This is also consistent with SEM/EDX results, which show the presence of Cu-rich phases, predominantly δ and, occasionally, θ, for alloy 1232, while alloy 12421 shows a large fraction of additional low melting point γ phase with up to 50 wt.% Cu content and qualitatively larger and more numerous θ particles.

The alloys studied were artificially aged and therefore show more significant variations, which agrees with literature. Toda et al. [9] obtained the Cu-distribution in an Al-Si-Cu alloy using a similar approach. It was found that the alloy exhibited the highest mechanical performance after solution annealing for 7.2 ks at 807 K attributed to homogenisation and the associated slower growth of micropores, which induce stress concentrations during tensile deformation. In contrary, the alloys studied do not exhibit a high degree of porosity induced by heterogeneities. Rather, an examination of the 3D elemental distribution in the post-mortem state reveals that intermetallics and inhomogeneities do have an influence on main crack propagation. The 2D slice in Fig. 5a) shows the intermetallics in which the Ni concentration is higher than Cu in green, while those with higher Cu concentration than Ni are shown in red. The main crack propagates through interfaces between these different types of intermetallics as indicated by the blue arrows and also the 3D visualization within the blue rectangle. Also, locations with apparent inhomogeneities in the Cu/Ni distribution within an intermetallic are repeatedly found to act as sites for crack deflection as indicated by the pink arrows and the corresponding 3D visualizations enclosed by blue and orange rectangles, probably due to a mismatch in deformation

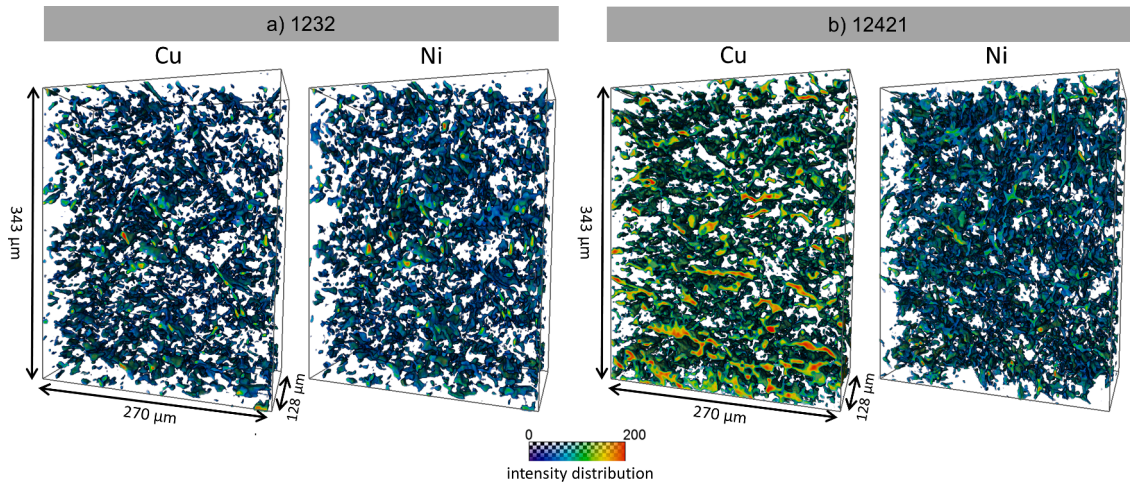

Fig. 4. Distribution of Cu (left) and Ni (right) for a) 1232 and b) 12421.

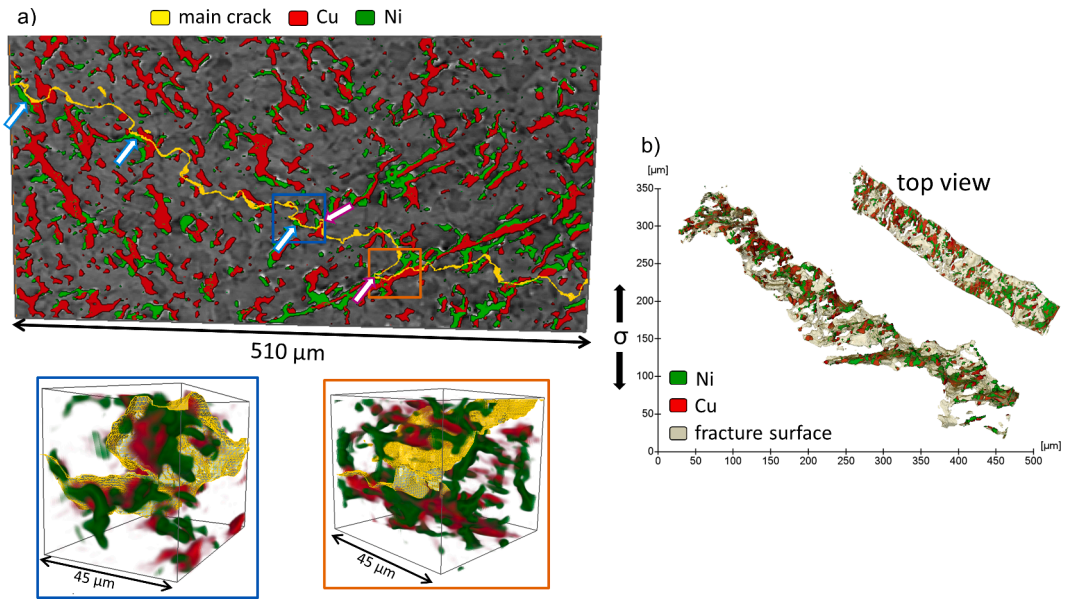

Fig. 5. a) correlation of 3D elemental distribution of Cu (red) and Ni (green) with main crack propagation (yellow) after tensile testing at RT, b) distribution of Cu- and Ni- rich intermetallics along the fracture surface.

behaviour between these regions. The fracture surface shown in Fig. 5b) indicates that the crack tends to propagate along large plate-like Al-Cu-Ni structures.

In conclusion, a combined study of the 3D elemental distribution, phase morphology and fracture behaviour of two cast near eutectic Al-Si alloys has been conducted. sAET revealed the Cu and Ni distribution. Inhomogeneous element distributions at the surface of intermetallics and Cu-rich and Cu-Ni-rich intermetallics adjacent to Cu-Ni-rich or Ni-Fe-rich intermetallics formed during earlier solidification sequences were observed. sXCT after RT tensile fracture showed that the main crack propagated along rigid phases rather than through the matrix. Crack propagation appears more likely to occur through interfaces between different Ni- and Cu-rich intermetallics. Local inhomogeneities in Cu/Ni distribution within intermetallics act as sites for crack deflection.

CRediT authorship contribution statement

Katrin Bugelnig: Data curation, Formal analysis, Investigation, Project administration, Validation, Visualization, Writing – original draft, Conceptualization, Funding acquisition. **Holger Germann:** Resources, Conceptualization. **Thomas Steffens:** Resources, Conceptualization. **Fabian Wilde:** Investigation. **Guillermo Requena:** Funding acquisition, Supervision, Writing – original draft, Writing – review & editing, Conceptualization.

Declaration of competing interest

The authors declare that they have no known competing financial interests or personal relationships that could have appeared to influence the work reported in this paper.

Acknowledgements

DESY is acknowledged for the provision of synchrotron facilities at the beamline P05.

Supplementary materials

Supplementary material associated with this article can be found, in the online version, at doi:10.1016/j.scriptamat.2024.116115.

References

[1] K. Bugelnig, H. Germann, T. Steffens, F. Sket, J. Adrien, E. Maire, E. Boller, G. Requena, Revealing the effect of local connectivity of rigid phases during deformation at high temperature of cast AlSi12Cu4Ni(2,3)Mg Alloys, Materials (Basel) 11 (8) (2018) 1300.
[2] K. Bugelnig, F. Sket, H. Germann, T. Steffens, R. Koos, F. Wilde, E. Boller, G. Requena, Influence of 3D connectivity of rigid phases on damage evolution during tensile deformation of an AlSi12Cu4Ni2 piston alloy, Mater. Scie. Eng. A 709 (2018) 193–202.
[3] G. Requena, G. Garcés, Z. Asghar, E. Marks, P. Staron, P. Cloetens, The effect of connectivity of rigid phases on strength of Al-Si alloys, Adv. Eng. Mater. 13 (2011) 674–684.
[4] Z. Asghar, G. Requena, E. Boller, 3D rigid multiphase networks providing high-temperature strength to cast AlSi10Cu5Ni1-2 piston alloys, Acta Mater. 59 (2011) 6420–6432.
[5] A.R. Farkoosh, M. Javidani, M. Hoseini, D. Larouche, M. Pekguleryuz, Phase formation in as-solidified and heat-treated Al–Si–Cu–Mg–Ni alloys: thermodynamic assessment and experimental investigation for alloy design, J. Alloys. Compd. 551 (2013) 596–606.
[6] X. Cao, J. Campbell, Morphology of -Al5FeSi Phase in Al-Si Cast Alloys, Mater. Trans. 47 (5) (2006) 1303–1312.
[7] Z. Asghar, G. Requena, F. Sket, Multiscale tomographic analysis of heterogeneous cast Al-Si-X alloys, J. Microsc. (2015) 1–9.
[8] Y. Liu, F. Meirer, J. Wang, G. Requena, P. Williams, J. Nelson, A. Mehta, J. C. Andrews, P. Pianetta, 3D elemental sensitive imaging using transmission X-ray microscopy, Anal. Bioanal. Chem. 404 (2012) 1297–1301.
[9] H. Toda, T. Nishimura, K. Uesugi, Y. Suzuki, M. Kobayashi, Influence of high-temperature solution treatments on mechanical properties of an Al–Si–Cu aluminum alloy, Acta Mater 58 (2010) 2014–2025.
[10] T. Nishimura, H. Toda, M. Kobayashi, T. Kobayashi, K. Uesugi, Y. Suzuki, Change in microstructure of Al–Si–Cu casting alloys during high temperature solution treatment, Int. J. Cast Metals Research 21 (1–4) (2008) 114–118.
[11] Q. Zhang, H. Toda, Y. Takami, Y. Suzuki, K. Uesugi, M. Kobayashi, Assessment of 3D inhomogeneous microstructure of highly alloyed aluminium foam via dual energy K-edge subtraction imaging, Philosoph. Magaz. 90 (14) (2010) 1853–1871.
[12] F. Wilde, M. Ogurreck, I. Greving1, J.U. Hammel, F. Beckmann, A. Hipp, L. Lottermoser, I. Khokhriakov, P. Lytaev, T. Dose, H. Burmester, M. Müller, A. Schreyer, Micro-CT at the imaging beamline P05 at PETRA III, AIP Conf. Proc. 1741 (2016) 030035.
[13] J. Moosmann, F. Wieland, B. Zeller-Plumhoff, S. Galli, D. Krüger, A. Ershov, S. Lautner, A Load Frame for in Situ Tomography at PETRA III, in: Proceedings of SPIE - Developments in X-Ray Tomography XII 11113, 2019.
[14] J. Schindelin, I. Arganda-Carreras, E. Frise, V. Kaynig, M. Longair, T. Pietzsch, A. Cardona, Fiji: an open-source platform for biological-image analysis, Nat. Methods 9 (7) (2012) 676–682, 2019.
[15] H. Toda, Applied Imaging Methods, X-Ray CT: Hardware and Software Techniques, Springer Singapore, Singapore, 2021, pp. 267–332. ISBN 978-981-16-0589-5.
[16] J.O. Andersson, T. Helander, L. Höglund, P.F. Shi, B. Sundman, Thermo-Calc and DICTRA, computational tools for materials science, Calphad 26 (2002) 273–312.
[17] N.A. Belov, D.G. Eskin, N.N. Avxentieva, Constituent phase diagrams of the Al–Cu–Fe–Mg–Ni–Si system and their application to the analysis of aluminium piston alloys, Acta Mater. 53 (17) (2005) 4709–4722.

[18] L.F. Mondolfo, Aluminum Alloys: Structures and Properties, Butterworth &Co (Publishers) Ltd, 1976. ISBN 0 408 70932 4.
[19] C.L. Chen, A. Richter, R.C. Thomson, Investigation of mechanical properties of intermetallic phases in multi-component Al–Si alloys using hot-stage nanoindentation, Intermetallics 18 (4) (2010) 499–508.
[20] R. Gholizadeh, S.G. Shabestari, Investigation of the effects of Ni, Fe, and Mn on the formation of complex intermetallic compounds in Al-Si-Cu-Mg-Ni alloys, Metall. Mater. Trans. A 42 (2011) 2011—3447.
[21] M. Warmuzek, Chemical composition of the Ni-containing intermetallic phases in the multicomponent Al alloys, J. Alloys Compd. 604 (2014) 245–252.
[22] H.Q. Liu, J.C. Pang, M. Wang, S.X. Li, Z.F. Zhang, Effect of temperature on the mechanical properties of Al–Si–Cu–Mg–Ni–Ce alloy, Mater. Sci. Eng. A 824 (2021) 141762.
[23] J.T. Kim, V. Soprunyuk, N. Chawake, Y.H. Zheng, F. Spieckermann, S.H. Hong, K. B. Kim, J. Eckert, Outstanding strengthening behavior and dynamic mechanical properties of in-situ Al–Al3Ni composites by Cu addition, Compos. Part B 189 (2020) 107891.